

Resonantly forced gravity–capillary lumps on deep water. Part 1. Experiments

JAMES D. DIORIO¹, YEUNWOO CHO²,
JAMES H. DUNCAN^{1†} AND T. R. AKYLAS²

¹Department of Mechanical Engineering, University of Maryland, College Park, MD 20740, USA

²Department of Mechanical Engineering, Massachusetts Institute of Technology,
Cambridge, MA 02139, USA

(Received 1 June 2010; revised 27 October 2010; accepted 14 November 2010)

The wave pattern generated by a pressure source moving over the free surface of deep water at speeds, U , below the minimum phase speed for linear gravity–capillary waves, c_{min} , was investigated experimentally using a combination of photographic measurement techniques. In similar experiments, using a single pressure amplitude, Diorio *et al.* (*Phys. Rev. Lett.*, vol. 103, 2009, 214502) pointed out that the resulting surface response pattern exhibits remarkable nonlinear features as U approaches c_{min} , and three distinct response states were identified. Here, we present a set of measurements for four surface-pressure amplitudes and provide a detailed quantitative examination of the various behaviours. At low speeds, the pattern resembles the stationary state ($U=0$), essentially a circular dimple located directly under the pressure source (called a state I response). At a critical speed, but still below c_{min} , there is an abrupt transition to a wave-like state (state II) that features a marked increase in the response amplitude and the formation of a localized solitary depression downstream of the pressure source. This solitary depression is steady, elongated in the cross-stream relative to the streamwise direction, and resembles freely propagating gravity–capillary ‘lump’ solutions of potential flow theory on deep water. Detailed measurements of the shape of this depression are presented and compared with computed lump profiles from the literature. The amplitude of the solitary depression decreases with increasing U (another known feature of lumps) and is independent of the surface pressure magnitude. The speed at which the transition from states I to II occurs decreases with increasing surface pressure. For speeds very close to the transition point, time-dependent oscillations are observed and their dependence on speed and pressure magnitude are reported. As the speed approaches c_{min} , a second transition is observed. Here, the steady solitary depression gives way to an unsteady state (state III), characterized by periodic shedding of lump-like disturbances from the tails of a V-shaped pattern.

Key words: bifurcation, solitary waves

1. Introduction

Solitary waves are locally confined nonlinear disturbances of permanent form, resulting from a perfect balance between the opposing effects of wave dispersion and

† Email address for correspondence: duncan@umd.edu

nonlinear steepening. These waves are prominent nonlinear features in free-surface and interfacial flows (see the review by Dias & Kharif 1999) as well as in various geophysical flow environments where stratification, shear and/or rotation are present (see, for example, Grimshaw 2007).

Since the original observation of a solitary wave by John Scott Russell in 1834 (see Russell 1844), the problem of water waves has served as motivation for many key advances in our understanding of solitary waves and related nonlinear wave phenomena. Most attention has been paid to solitary waves on shallow water, which bifurcate from a uniform stream at the linear-long-wave speed and are governed by the Korteweg–de Vries (KdV) equation in the small-amplitude limit (Whitham 1974, §13.11). Apart from being the bifurcation point of KdV solitary waves, the long-wave speed, c_0 , is also associated with a resonance condition: the linear response to external forcing moving at this critical speed grows unbounded in time (Akylas 1984). Naturally, nonlinear effects are important near this resonance, and the forced response due to a pressure disturbance on the free surface or a bottom bump travelling with speed close to c_0 involves periodic shedding of KdV solitary waves (Akylas 1984; Cole 1985; Wu 1987).

The KdV equation applies to two-dimensional (plane) waves and is replaced by the Kadomtsev–Petviashvili (KP) equation when variations in the transverse direction are taken into account (see, for example, Akylas 1994). The KP equation reveals that fully localized three-dimensional solitary waves, or ‘lumps’, are not possible on shallow water under typical flow conditions. On physical grounds, for a lump to remain locally confined, its speed must be such that no linear wave can co-propagate with the main wave core; this condition is satisfied when the speed at which lumps bifurcate coincides with a minimum of the linear phase speed, lumps thus being found below this minimum. In shallow water, however, c_0 is a maximum of the phase speed of pure gravity waves. Moreover, for shallow-water gravity–capillary waves, c_0 becomes a phase-speed minimum if surface tension τ is sufficiently strong: $\tau > \frac{1}{3}\rho g H^2$, H being the water depth, ρ being the fluid density and g being the gravitational acceleration; however, this condition restricts H to less than a few millimetres.

The situation is entirely different for gravity–capillary waves on deep water. Ignoring viscous dissipation, the phase speed now features a minimum, $c_{min} = \sqrt{2}(\tau g/\rho)^{1/4}$, at the non-zero wavenumber $k_{min} = (\rho g/\tau)^{1/2}$. (In cgs units, $\tau = 73$, $\rho = 1$ and $g = 981$, so $c_{min} = 23 \text{ cm s}^{-1}$ and $\lambda_{min} = 2\pi/k_{min} = 1.71 \text{ cm}$.) This minimum is the bifurcation point of a new class of two-dimensional (plane) gravity–capillary solitary waves as well as lumps, and the latter turn out to be the most relevant physically.

Specifically, at c_{min} , two branches of two-dimensional solitary waves bifurcate from linear sinusoidal waves of wavenumber k_{min} , one of elevation and the other of depression, and they propagate at speeds less than c_{min} . In the small-amplitude limit slightly below c_{min} , both types of two-dimensional solitary waves behave as modulated wavepackets with carrier wavenumber k_{min} (Akylas 1993; Dias & Iooss 1993; Longuet-Higgins 1993), and at finite steepness, depression solitary waves transform into isolated troughs (Longuet-Higgins 1989; Vanden-Broeck & Dias 1992). However, only the depression branch is stable to longitudinal perturbations (Calvo & Akylas 2002), and these solitary waves turn out to be unstable, too, in the presence of transverse perturbations (Kim & Akylas 2007).

The minimum gravity–capillary phase speed, c_{min} , is also the bifurcation point of elevation and depression lumps propagating at speeds less than c_{min} (Kim & Akylas 2005; Părău, Vanden-Broeck & Cooker 2005; Akers & Milewski 2009). These fully localized steady solutions share several common features with their two-dimensional counterparts. Lump profiles, in particular, are relatively elongated in the transverse

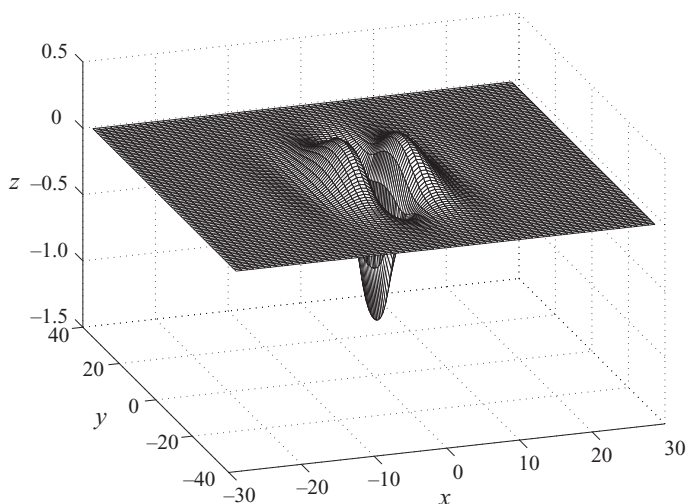


FIGURE 1. Profile of the deep-water gravity–capillary lump solution of potential flow theory, computed with boundary-element methods (from Părău *et al.* 2005, their figure 1). The lump is propagating in the x -direction with speed $0.917 c_{min}$. The vertical scale is expanded by a factor of 20.

direction and resemble qualitatively two-dimensional solitary-wave profiles along the propagation direction (figure 1). With regard to their stability properties, however, lumps behave very differently from two-dimensional solitary waves: while both lump-solution branches are unstable in the small-amplitude limit, lumps of depression become stable at finite steepness (Akylas & Cho 2008). This suggests that, if viscous dissipation is somehow overcome, steep depression gravity–capillary lumps are likely to be observable. In fact, unsteady numerical computations using an undamped model equation indicate that the transverse instability of depression two-dimensional solitary waves results in the formation of finite-amplitude depression lumps (Kim & Akylas 2007).

In contrast to the progress made in the theory of two-dimensional gravity–capillary solitary waves and lumps on deep water, there have been only a few related experimental studies. In laboratory-scale wind-wave experiments, Zhang (1995) observed isolated features with sharp curvatures in slope images of the water surface. The features were relatively elongated in one direction, resembling, at least qualitatively, theoretically predicted shapes of lumps. Measurements of the profiles across the narrow dimension of these features showed reasonable agreement with computed profiles of two-dimensional solitary waves in Longuet-Higgins (1989). In a later laboratory experiment, Longuet-Higgins & Zhang (1997) used a two-dimensional slit to create a vertically oriented air jet that impinged on the water surface in a recirculating water channel. The plane of the jet was normal to the flow direction and a small amount of chalk powder was used to make the free surface visible. When the free-stream water velocity was below c_{min} , a localized wave formed directly beneath the impinging jet. The shape of the free surface showed good agreement with computed two-dimensional solitary gravity–capillary waves (Longuet-Higgins 1989), but the wave pattern was not completely steady owing to lateral instabilities, particularly at lower speeds.

The present and the following companion paper (Cho *et al.* 2011) are devoted to a combined experimental and theoretical investigation of gravity–capillary lumps,

generated by a localized pressure source moving over deep water at speeds below c_{min} . Similar to c_0 in shallow water, c_{min} is a critical forcing speed at which the linear inviscid response becomes singular (Raphaël & de Gennes 1996), and nonlinear effects as well as viscous dissipation are expected to come into play as this resonance is approached. In earlier work, assuming potential flow, Părău *et al.* (2005) computed the steady-state wave pattern induced by a localized pressure disturbance moving on the free surface of deep water; as c_{min} is approached from below, the response, rather than blowing up as predicted by linear theory, turns around at a certain critical speed less than c_{min} , forming a limit point, and then follows a finite-amplitude solution branch corresponding to essentially free lumps of depression. Calvo & Akylas (2002) examined the stability of this steady-state forced response and found that only the small-amplitude (Rayleigh's) solution branch is stable, suggesting that this state would be realizable for forcing speeds below the limit point. What happens for forcing speeds above the critical speed defined by the limit point, and the possible role of lumps, are open questions that will be addressed in the present investigation.

A related issue is the role of viscous dissipation, which is known to be significant for waves in the gravity–capillary range (Lamb 1993, §348). In their more recent steady-state computations, Părău, Vanden-Broeck & Cooker (2007) introduced a small damping term in the dynamic free-surface condition merely as a device for imposing the radiation condition. We find that, as the forcing speed is increased towards c_{min} , the response is not always steady; moreover, its precise nature is decided by a delicate balance between nonlinearity, which is controlled by the strength of forcing, and viscous dissipation.

Part 1 of this work is an experimental study of the surface wave pattern due to a circular surface pressure distribution (created by blowing air onto the water surface) translating at constant speeds less than c_{min} . In an earlier preliminary publication (Diorio *et al.* 2009), photographs of the surface deformation pattern and measurements of its maximum depth as a function of translation speed for a single air flow rate were presented. Three distinct response states were found, one of which clearly resembled a deep-water gravity–capillary lump. In the present paper, an extensive set of measurements of these phenomena is described, including the three-dimensional shape of the steady-state response. A detailed comparison of the experimental observations with a theoretical model is made in Part 2 of this work.

2. Experimental details

2.1. Experimental set-up

The experiments were carried out in a tank that is 7.3 m long, 0.76 m wide and 0.91 m deep (see figure 2). The sides and bottom of the tank were made of glass to allow optical access. The tank includes an instrument carriage that rides on precision rails mounted on top of the long sidewalls of the tank. This carriage is towed by a wire rope that is driven by a servo-motor. The rotation rate of the motor is measured by an optical encoder and controlled by a servo-motor drive unit that includes a motor-speed feedback loop. A linear displacement sensor was used to monitor the carriage position as a function of time during each experimental run. An analysis of the records from this sensor revealed that the carriage speed varied by less than 0.3 % from the average speed during an individual run, and that the average speed varied by less than 0.01 % from run to run.

Since maintaining a water surface that is relatively free of surfactants is critical to the present experiments, the following procedures were implemented. Before each series

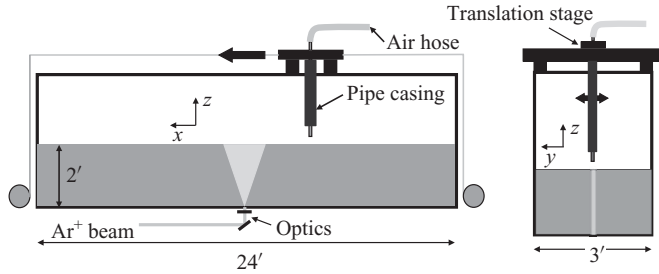


FIGURE 2. Schematic diagram of the experimental set-up. A small tube (2.5 mm ID) is mounted in a vibration-reducing casing and attached to a movable carriage. A pressurized air line forces air through the tube to generate a small depression on the water surface. A high-speed camera (not shown) images the water surface deformation pattern from the side. The tube is towed in the x (streamwise) direction and is mounted on a translational stage so that it can be displaced in the y (cross-stream) direction.

of experiments, the tank was filled with filtered tap water to a depth of approximately 60 cm. Chlorine was then added to the water at a concentration of approximately 10 p.p.m. in order to minimize the presence of organic materials and the surfactants that they produce. The tank includes a surface skimmer and filtration system that skims water from the free surface at one end of the tank, pumps it through a diatomaceous earth filter and returns it back into the tank at the end opposite to the skimmer. This filtration system was run for several hours before the experiments began. However, in order to minimize the effects of background fluid motion, the skimmer–filtration system was turned off while the measurements were taken. The surface tension τ was measured *in situ* using a Wilhelmy plate device located at the end of the tank opposite to the skimmer. It was found that after the skimmer–filtration system was run for 30 min or more and then turned off, the surface tension was equal to the clean water value, 73 dyn cm^{-1} , and remained at this value for about 45 min. Given the above data, the experiments were performed using the following procedure. First, the skimmer–filtration system was turned on for a period of at least 30 min. Then, the skimmer–filtration system was turned off and the surface tension was measured. The experiments were then run repeatedly for 30 min, at which time the surface tension was measured again and the skimmer–filtration system was turned on. In all cases, the measured surface tension before and after the 30 min series of experiments was found to be 73 dyn cm^{-1} . For this value of surface tension and water depth $H = 60 \text{ cm}$, the Bond number $B = \tau/\rho g H^2 \ll 1$, corresponding to the deep-water limit, where the minimum phase speed $c_{\min} = 23 \text{ cm s}^{-1}$ and the wave number at the minimum phase speed $k_{\min} = 3.66 \text{ cm}^{-1}$ (see §1).

A pressure disturbance was created on the water surface by blowing air through a small-diameter tube. The tube has an inside diameter $D = 2.5 \text{ mm}$ and was secured with silicone in a slot between two aluminium plates and mounted to the carriage with vibration-reducing bushings to minimize tube shaking when the carriage was moving. The tube was oriented vertically above the water surface with its lower end positioned 1 cm above the mean water level. A pressurized airline was then connected to the other end of the tube. The air flow through this line was controlled using a variable area flow meter (King Gage) with an accuracy of 6% of the full-scale flow (2.4 l min^{-1}).

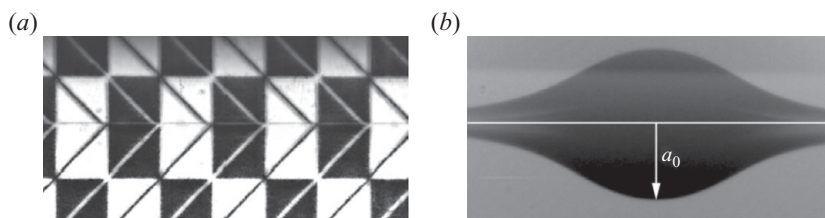


FIGURE 3. (a) Image of the checkerboard calibration target ($3.175 \times 3.175 \text{ mm}^2$) with diagonals used to locate the undisturbed free surface. The horizontal line where the diagonals change from positive to negative slope is probably the contact line of the water on the checkerboard as seen from below the water surface. The part of the image above this line is a reflection of the submerged portion of the checkerboard. Because of the positive meniscus at the contact line, the diagonals seen below the water surface and in the reflection do not meet at the contact line. The location of the free surface was taken as the intersection of straight lines fitted by eye to the upper and lower diagonals in the image. (b) Shadowgraph image of the dimple for an air flow rate corresponding to $\epsilon = 0.43$ taken with the carriage stationary. The horizontal line is an estimate of the location of the free surface. The portion of the image above this line is a reflection of the part below the line. The parameter a_0 is the maximum depth of the dimple. Because of differences in image cropping and magnification, the mean water level does not appear to be at the same height in the two images.

2.2. Measurement details

All of the water surface profile measurements were photography based and used a high-speed digital movie camera (Phantom 9, Vision Research, 1632×800 pixel images), which was positioned on the outside of the tank and viewed the air-jet tube and water surface from the side. The camera was either attached to a tripod that was fixed to the laboratory floor or attached to the carriage that carried the air-jet tube. In cases where the camera was attached to the carriage, the camera and its lens were first connected to a custom-made 12.7 mm-thick aluminium plate to stabilize the lens relative to the camera. This plate was then attached to a ball-mount tripod head (Arca Swiss Monoball) that was attached to the carriage using vibration-isolation bushings in order to minimize camera vibration when the carriage was moving. The camera was focused on a vertical plane near the centre of the air-jet tube and calibrated using an image of a vertically oriented ‘checker-board’ target (see figure 3a). For these experiments, one pixel corresponded to roughly 0.02 mm in the physical plane.

In order to make the free surface visible to the camera, two different techniques were used: backlighting and laser-induced fluorescence (LIF). When using the backlighting technique, translucent screens were attached to the wall of the tank opposite to the camera and illuminated from behind with white light in order to create a uniform bright background. With this light source in place, the camera was set to view the surface from either above or below the mean water level, depending on the desired information. When viewing the surface from above the mean water level, the camera had a look down angle of roughly 10° and deformations in the free surface appear as bright and dark areas in the high-speed movies. These above-surface images yield an excellent qualitative picture of the surface pattern, including the general three-dimensional shape, but do not yield quantitative data such as surface height. When viewing the free surface from below, the line of the sight of the camera was horizontal and located approximately 0.5 cm below the mean water level. In this configuration, the images are essentially shadowgraphs and surface depressions appear dark because the curved air–water interface deflects the white light coming from the translucent

screen. These images are a projection of the three-dimensional surface depression and are excellent for determining the maximum depth of the depression.

An accurate measure of the mean water level is crucial to measurements of the depth of the depression. To this end, the above-mentioned checkerboard pattern included diagonal lines (see figure 3a). As can be seen in the image, the diagonals seen below the water surface and their reflection in the underside of the water surface between the checkerboard and the camera in the top part of the image are oriented at 90° to one another. The water surface in the focal plane of the camera is near the intersection of these sets of diagonal lines. Close examination of the image shows that the lines do not meet at the reflection point. This is due to the meniscus on the checkerboard. Thus, the location of the free surface was taken as the intersection of straight lines fitted by eye to the upper and lower diagonals in the image. We estimate that the location of the free surface can be determined to within ± 5 pixels with this method, or about 0.1 mm in the physical plane. While both the above-surface and below-surface images have their limitations, the information from each can be considered together to understand and quantify the wave behaviour. Both of these types of back-lighted images were taken with the camera fixed to the tripod and mounted on the carriage. This latter configuration was used to record any time-dependent behaviour in the surface shape.

In the LIF technique, fluorescein dye was added to the water at a concentration of less than 5 p.p.m. and a laser light sheet from a 1-watt argon-ion laser was projected onto the water surface vertically from under the tank. The water level was set to about 15 cm, corresponding to essentially deep water (Bond number $B = 0.00033$). The light sheet was about 5 cm wide and 0.01 cm thick at the undisturbed water surface, remained stationary and was oriented so that its long axis was in the direction of the carriage motion (i.e. the x or streamwise direction). The camera imaged the intersection of the laser sheet and the water surface from the side with a look-down angle of about 20° and a frame rate of 500 p.p.s. Images of a checker-board grid placed in the plane of the light sheet were used for calibration. The camera remained stationary and recorded images of the surface deformation as the air-jet tube passed by. These images were then processed using standard image edge-detection algorithms in MATLAB to obtain the water surface profile. The accuracy of the edge detection depends upon the quality of the image and the spatial resolution of the camera set-up. For the well-focused images obtained in these experiments, the free surface can typically be located to within 1–2 pixels (0.02–0.04 mm in the physical plane). The height of the free surface in one column of pixels near the centre of the image was tracked as a function of time, which yielded, after calibration, water surface height as a function of time, $z(t)$. Assuming the wave pattern to be steady (as it was for the parameter range in which the LIF technique was used) this temporal information could be converted to $z(x)$, where x is the streamwise coordinate in the reference frame moving with the air-jet tube, by using $x = Ut$, where U is the carriage speed and t is time as measured from the image number and the time between images, 1/500 s. This point-tracking method was particularly useful for obtaining a ‘wide’ view of the surface since the movie captures an effective width around the air-jet tube that is much greater than the field of view of a single image. (For an air-jet tube velocity of $U = 23 \text{ cm s}^{-1}$ and a data record of 1000 images, the effective ‘field of view’ of the data is 46 cm.) Because the air-jet tube was mounted on a translation stage, it could be accurately displaced in the cross-stream (y) direction relative to the light sheet. Repeating runs with the tube at different y -locations and one experimental condition yielded a number of $z(x)$ profiles that could be combined together to form a detailed three-dimensional, $z(x, y)$, map of the surface pattern.

Because the LIF method reconstructs the surface pattern from several data runs, successive movies must be temporally registered relative to one another; i.e. the position of the tube in say frame number 500 must be nearly the same in every run. To this end, a camera trigger system was built using a low-power laser that was pointed horizontally across the 0.76 m width of the tank at a photo-diode. When the air-jet tube passed through this laser beam, an electric circuit was triggered by the diode and this circuit in turn triggered the movie camera. In order to test the repeatability of this trigger system, the high-speed camera was set to record the passage of the air-jet tube, using white light for illumination. The location of the leading edge of the tube at a given movie frame of the sequence was measured using standard edge-detection techniques. A series of runs showed that the location of the tube in the movie frame was repeatable to within 0.5 mm ($\approx 1/5$ tube diameters) from run-to-run. As will be shown below, this repeatability was sufficient for reconstruction of the three-dimensional wave pattern.

It should be kept in mind that the three-dimensional pattern is created from slices of height versus time (converted to x) at constant values of y , which are spaced by a distance of 2.5 mm. Given that the inside diameter of the air-jet tube is 2.5 mm, the three-dimensional pattern is not well resolved in y . In spite of this relatively coarse resolution in y , the LIF technique yields a good measurement of the shape of the pattern in the horizontal plane.

2.3. Experimental conditions

In each experimental run, the air flow was turned on and then about one minute later the carriage motion, consisting of a period of constant acceleration, a period of constant speed U and a period of constant deceleration, began. The speed U ranged from roughly 16–24 cm s^{-1} , which corresponds to a range of dimensionless speeds $\alpha = U/c_{\min}$ from 0.7 to 1.03. The acceleration was 10 cm s^{-2} and the total distance travelled by the carriage was 3.81 m in all runs. Subtracting the distance travelled during the acceleration and deceleration phases, the carriage travelled 3.24 m over a time of 13.55 s at the maximum speed used in this study, $U = 23.9 \text{ cm s}^{-1}$. Four air-flow rates ranging from 0.95–1.9 l min^{-1} were used. We define a non-dimensional forcing parameter, $\epsilon = a_0/D$, where a_0 is the maximum depth of the depression created by the air pressure when the carriage was stationary and D is the inside diameter of the air-flow tube. The four air-flow rates correspond to $\epsilon = 0.30, 0.43, 0.51$ and 0.69. The stationary depression depth a_0 was measured using the shadowgraph images as described above (see sample image in figure 3*b*). A series of measurements showed a variation in a_0 of about 5% of the mean from run-to-run for a given air-flow rate. The source of this variation is most probably due to the combination of the errors in the repeatability of setting the air-flow rate and errors in determining the mean water level in the images.

3. Results and discussion

3.1. Behavioural states and the critical jump condition

The qualitative shape of the surface deformation pattern for one value of $\epsilon = 0.43$ and six towing speeds $\alpha = U/c_{\min}$ ranging from 0.905 to 1.03 can be seen in the six images in figure 4. For these images, the camera viewed the water surface from above the mean water level and backlighting was used for illumination as described in §2.2. The air-jet tube, and hence the surface pressure distribution, is moving from right to left. The light and dark patterns are caused by ridges and depressions of various

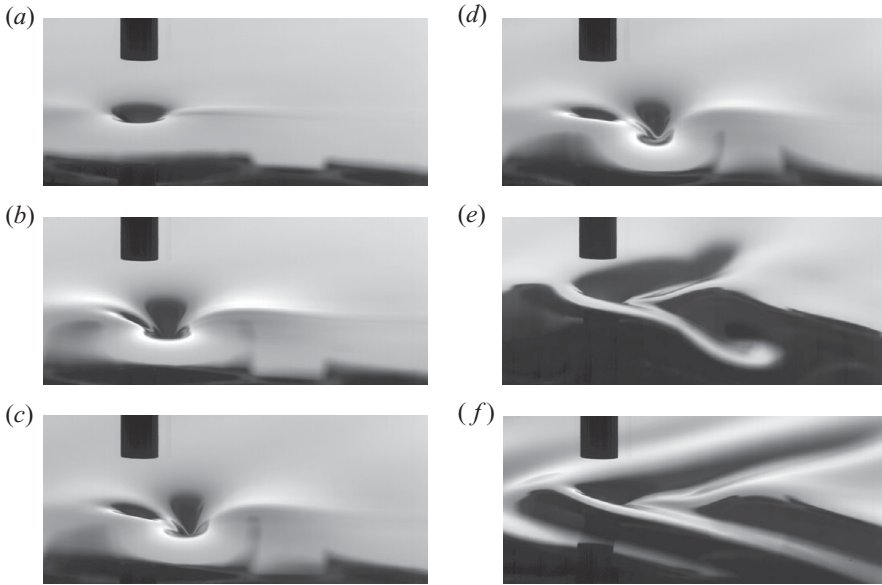


FIGURE 4. Images of the wave pattern taken from above the water surface with the high-speed camera. The forcing parameter is approximately $\epsilon = 0.43$. The air-jet tube is moving from right to left. (a) $\alpha = 0.905$, (b) $\alpha = 0.927$, (c) $\alpha = 0.948$, (d) $\alpha = 0.970$, (e) $\alpha = 0.981$, (f) $\alpha = 1.03$. For scale, note that the outside diameter of the air-jet tube (located in the upper left of each image) is 3.2 mm. From Diorio *et al.* (2009).

slopes and curvatures. Roughly speaking, the light (dark) areas represent regions of the surface where reflection and refraction at the water surface directs the light towards (away from) the camera. For scale, note that the outer diameter of the air-jet tube (visible in the photographs) is 3.2 mm.

At the lowest towing speed shown (figure 4a), $\alpha = 0.905$, there is a depression located directly beneath the air jet. This depression is nearly axisymmetric about the tube centreline and resembles the depression seen when the carriage is stationary. We refer to this surface response as state I and it occurs from $\alpha = 0$ to a critical value of $\alpha_c \approx 0.9$. As α is increased beyond α_c , a single isolated wave forms behind the local depression directly under the air-jet tube (figure 4b, $\alpha = 0.927$). This trailing wave is elongated in the cross-stream direction and is many times wider than the diameter of the local depression. As α is increased further, this same trailing wave is observed; however, it gradually migrates farther and farther behind the surface pressure, as in figure 4(c, d). Although it is difficult to quantify from these images alone, figure 4(b–d) indicates that the depth of this trailing wave may be decreasing as the towing speed increases, as evidenced by the gradual increase in the grey level of the trailing depression. Because the surface response in figure 4(b–d) is markedly different from that at lower speeds, we refer to this asymmetric surface response as state II. As the towing speed approaches c_{min} , the trailing wave configuration begins to break down and stretch out into a V-shaped pattern (figure 4e). The surface response in this region of the parameter space is highly unsteady, and the ‘V’ shape appears to grow and contract. This time-dependent state is referred to as state III and will be discussed in more detail in § 3.3. Finally, for towing speeds above $\alpha = 1.0$ (i.e. $U > c_{min}$), the air jet creates a steady V-shaped wave pattern (figure 4f). This is similar to the response predicted by linear theory.

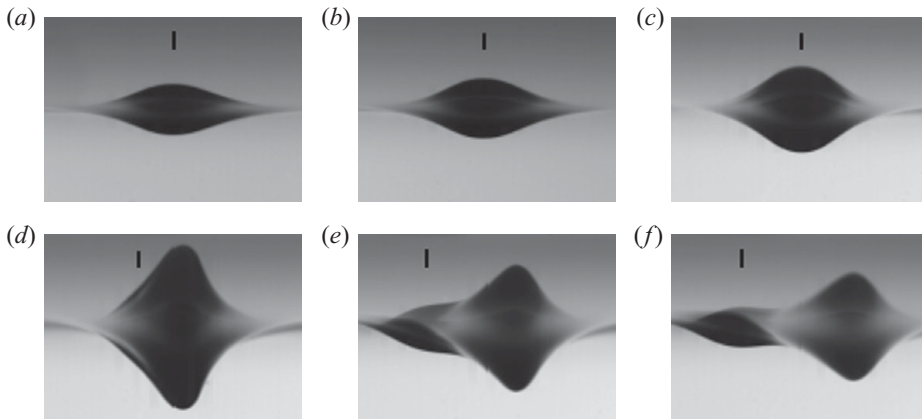


FIGURE 5. Shadowgraph images showing the shape of the wave pattern for several values of the speed parameter α for $\epsilon = 0.43$. The images are taken from slightly below the water surface so the top half of the image is a reflection of the lower half. In all cases, the tube is moving from right to left. The black lines denote the approximate position of the air-jet tube when the photograph was taken. Each image is roughly 9.5×7 mm in the physical plane. (a) $\alpha = 0.73$, (b) $\alpha = 0.82$, (c) $\alpha = 0.90$, (d) $\alpha = 0.90$, (e) $\alpha = 0.92$, (f) $\alpha = 0.95$. The panels (a–f) correspond to the letters on the curve in figure 6.

While the images in figure 4 highlight the qualitative changes in the surface response as a function of α , it is difficult to obtain quantitative measurements from them because the observed light patterns are the result of uncalibrated reflection and refraction processes. Therefore, shadowgraph images of the wave pattern were taken with the camera oriented horizontally and its optical axis positioned slightly below the mean water level, as described in § 2.2. A set of images taken using this method is shown in figure 5. In these images, the dark areas are regions where the free surface has dipped below the mean water level. Because the camera views the wave pattern from slightly below the mean water level, the top half of the image is a reflection of the lower half as seen in the underside of the water surface between the camera and the wave pattern. In all of these images, the air-jet tube is moving from right to left and the camera is stationary. Although it is not shown in these cropped images, the air-jet tube is visible in the full images and its approximate position is marked by a vertical line in each image in figure 5. The position of the tube is only known approximately because it is out of focus in the images. This problem is due to the differing optical path lengths between the camera and the surface depression, which is seen through water, and the camera and the tube, which is seen through air. The camera is focused on the surface depression.

For the images in figure 5, $\epsilon = 0.43$ and $0.73 \leq \alpha \leq 0.95$. In the top row of images (figure 5a–c), $\alpha = 0.73, 0.82$ and 0.90 , respectively, the pattern is a single depression with upstream/downstream symmetry centred on the tube location. The depression shape resembles the case when the tube is stationary (see figure 3b). These are examples of state-I responses. One can see that the maximum depth of the depression increases slightly as the towing speed is increased. The bottom row of images (figure 5d–f) shows the shape of the surface depression for $\alpha = 0.90, 0.92$ and 0.95 , respectively. The pattern is now asymmetric with respect to the streamwise direction and the deepest point is located downstream of the tube location. Note also that the location of the deepest point moves farther behind the tube and decreases in depth as the towing speed is increased, observations commensurate with the images in figure 4(b–d).

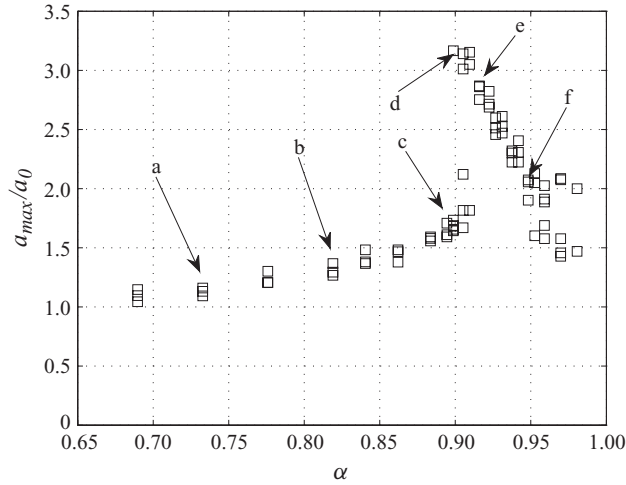


FIGURE 6. Normalized maximum depth of the wave pattern, a_{max}/a_0 , versus $\alpha = c/c_{min}$ for $\epsilon = 0.43$. Each data point is taken from a separate experimental run. The data points marked by letters correspond to the images in figure 5. Many of the data points were also presented in Diorio *et al.* (2009).

These are all examples of state-II responses. The transition between states I and II is abrupt; a small change in α can yield a dramatically different response. In fact, the two images in figure 5(c,d) are from separate experimental runs with the same value of α , indicating that at some speeds there may even be a bimodal behaviour. (The above-surface shadowgraph image in figure 4a also shows a state-I response at one of these bimodal points.)

To further investigate the surface deformation pattern, images such as those in figure 5 were used to measure the maximum depth of the pattern, a_{max} , for a wide range of α . This depth was then normalized by the depth of the depression when the tube was stationary, a_0 . A plot of a_{max}/a_0 versus α for the case with $\epsilon = 0.43$ is shown in figure 6. Note that the quantity a_{max}/a_0 is being reported as positive. Each data point in figure 6 represents a measurement of a_{max} taken as the air-jet tube passed by the location of the stationary camera in a separate experimental run. The data show that, at low speeds, the depression depth is a little greater than a_0 and gradually increases with increasing speed. The run-to-run variations in a_{max}/a_0 in this region, say for $\alpha < 0.88$, are quite low and the shape of the depression is highly repeatable. At a critical speed α_c , with $\alpha_c \approx 0.9$ for this ϵ , there is a sudden jump in a_{max}/a_0 . Points before this jump (i.e. on the lower curve) are always observed to be in state I while the points after the jump (i.e. on the upper curve) are observed to be in state II. This conclusion is supported by the shadowgraph images in figure 5(a-f), which were taken at the points marked by the corresponding letters in figure 6. In state II, a_{max}/a_0 decreases with increasing α .

For values of α near α_c , the run-to-run variation in a_{max}/a_0 increases dramatically. Take, for example, the four runs with α slightly less than 0.9; in three of these runs the pattern was observed to be in state I, while in one it was observed to be in state II. This overlap between the two branches of the curve occurs between approximately $\alpha = 0.895$ and 0.91. It is interesting to ask whether the surface pattern is always in a single state during one of these runs or whether it oscillates between the two states. This question is explored in more detail in § 3.3, where the movie camera is used to

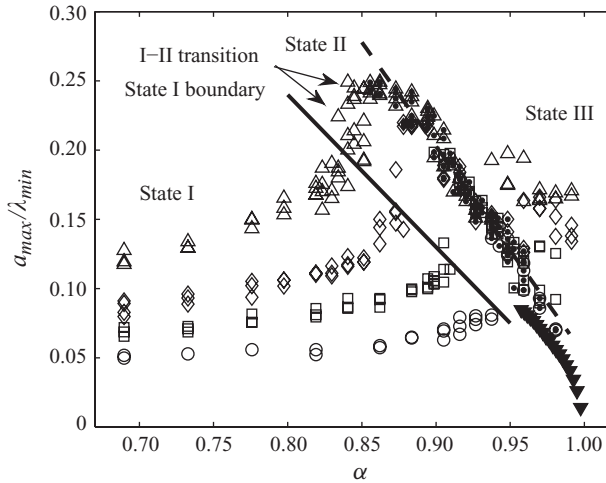


FIGURE 7. Normalized maximum depth of the wave pattern, a_{max}/λ_{min} , versus the speed parameter α . Data taken with four values of ϵ are shown: \circ , $\epsilon = 0.30$; \square , $\epsilon = 0.43$; \diamond , $\epsilon = 0.51$; and \triangle , $\epsilon = 0.69$. Note that all the data fall on a common line in state II (each of these data points is filled with a black dot in the centre), independent of the value of ϵ . The straight dashed line, $a_{max}/\lambda_{min} = -1.51\alpha + 1.56$, is a least-squares fit to the points considered to be in state II. Open data points at and above this line at high values of α are in state III (see text). The data points marked with \blacktriangledown are theoretical values from inviscid, freely propagating lump solutions computed by E. Părău (personal communication 2010).

record the temporal behaviour of the surface pattern in the reference frame of the air-jet tube. A broader scatter in the a_{max}/a_0 versus α data begins to emerge again as $\alpha \rightarrow 1$ (see the several points for $\alpha \approx 0.975$ in figure 6). These data points correspond to a state-III response as shown in figure 4(e). This behaviour will also be examined in §3.3.

The effects of varying ϵ , which is controlled by the surface pressure induced by the air jet, on the surface deformation pattern were also investigated. Some aspects of these effects are shown graphically in the plot of a_{max}/λ_{min} versus α in figure 7. Data are presented for all four values of ϵ : 0.30, 0.43, 0.51 and 0.69. Qualitatively, regardless of the value of ϵ , the surface response and the general shape of the curves of a_{max}/λ_{min} versus α resemble the case discussed above, $\epsilon = 0.43$ included in figure 7. However, the details of the a_{max}/λ_{min} versus α curves show considerable variation from one value of ϵ to another. As can be seen from the figure, the value of α_c and the jump in a_{max} at this α decrease with increasing ϵ , while the jump zone occurs over a wider range of α . Also, the value of α where the state-III response begins decreases with increasing ϵ . However, one of the most significant features of the plot is that the state-II data points for all four values of ϵ fall on a single curve. The dashed line in the plot is a least-squares fit of a straight line to the state-II data and is given by $a_{max}/\lambda_{min} = -1.51\alpha + 1.56$. Similarly, a monotonically decreasing relationship between the depth of the depression and increasing phase speed is found in the theory of freely propagating deep-water lumps, and results from recent numerical computations by E. Părău (personal communication 2010), assuming steady potential flow, are also given in figure 7.

3.2. Three-dimensional shape (states I and II)

Quantitative measurements of the three-dimensional shape of the surface deformation pattern were made with the LIF technique described in §2.2. For reasons mentioned

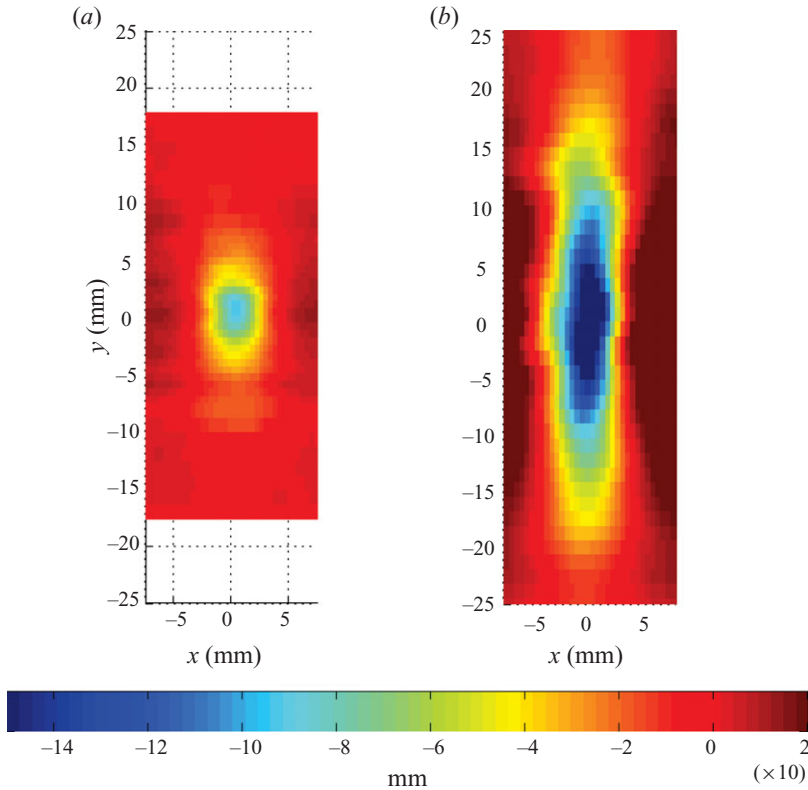


FIGURE 8. Contour plots (x - y plane) of the surface deformation pattern for $\epsilon = 0.43$ and two values of α . (a) $\alpha = 0.86$ and (b) $\alpha = 0.95$. The air-jet tube is moving from right to left. The data are obtained by tracking the height of the water surface at a single horizontal point in the movie image sequence as the wave pattern passes by. Each data sequence along a line of constant y is obtained from a different run with the air-jet tube at a different cross-stream (y) location relative to the laser light sheet.

there, this technique can only be used in states I and II where the pattern is steady. Figure 8(a,b) shows two contour plots of the water surface height $z(x, y)$ for $\epsilon = 0.43$ and two values of $\alpha = 0.86$ and 0.95 , respectively. The pressure source is moving from right to left and is located on the $y = 0$ axis in both plots. For $\alpha = 0.86$, the surface pattern is nearly circular and is centred under the air-jet tube (not shown in the figure). By these circular contours and the location of the point $\alpha = 0.86$ in the plot of a_{max}/a_0 versus α in figure 6, this is clearly a state-I response. Between $\alpha = 0.86$ (figure 8a) and $\alpha = 0.95$ (figure 8b), there is a marked increase both in the depth and the cross-stream width (about 40 mm) of the surface pattern. One can see some evidence of the small depression under the air-jet tube in the slight bulge in the upstream section of the contours along the centreline of the pattern. This is clearly a state-II response.

Figure 9 shows a perspective view of the surface, $z(x, y)$, for $\epsilon = 0.43$ and $\alpha = 0.95$, the same conditions as in figure 8(b). The tube motion is in the negative x -direction and the z -coordinate is magnified by a factor of 10. The plot is much wider in the x -direction than the contour plots in figure 8 and gives an excellent view of both the positive ridges on the upstream and downstream edges of the depression as well

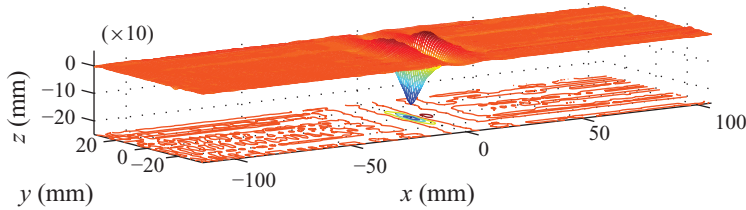


FIGURE 9. A perspective plot of the water surface for $\epsilon = 0.43$ and $\alpha = 0.95$. The vertical axis is scaled by a factor of 10 relative to the x - and y -axes. The data are obtained by tracking the height of the water surface at a single horizontal point in the movie image sequence as the wave pattern passes by. Each profile in the x - z plane is obtained from a different run with the air-jet tube at a different y -location. The smooth variation of the pattern in the y -direction is indicative of the repeatability and steadiness of the wave pattern.

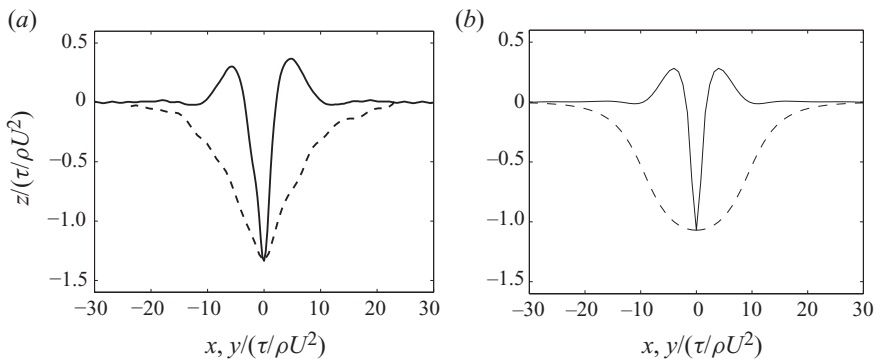


FIGURE 10. Streamwise (solid) and cross-stream (dashed) profiles at the centre of the surface deformation pattern. The two curves have been centred around zero on the abscissa for clarity. (a) Profiles from the present experiments, $\epsilon = 0.43$, $\alpha = 0.95$, corresponding to figure 8(b). (b) Profiles from calculations of freely propagating lumps at $\alpha = 0.919$, due to Părău *et al.* (2005, their figure 4a).

as showing that there were no measurable waves far upstream and downstream of the depression. The surface shows a three-dimensional pattern that is highly localized in all directions, elongated in the cross-stream relative to the streamwise direction, and very clearly resembles the gravity–capillary lump solutions computed by previous authors (figure 1).

The asymmetry of the surface deformation pattern in state II is shown more clearly in figure 10(a), which contains plots of the streamwise and cross-stream profiles at the centre of the wave pattern. The two curves have been shifted along the x - and y -axes so that the minima occur at $(x, y) = (0, 0)$. The streamwise profile shows a slight asymmetry, with the elevation of the leading (left) edge smaller than the trailing edge. This is probably due to the presence of the local depression under the air-jet tube. For comparison, the corresponding profiles from calculations of a freely propagating lump with $\alpha = 0.919$ by Părău *et al.* (2005) are shown in figure 10(b). As presented in non-dimensional coordinates, the two sets of profiles show a remarkable similarity in both shape and magnitude, despite the fact that they are for different values of α and the present results are forced while the results of Părău *et al.* (2005) are for freely propagating inviscid lumps. The experimentally observed streamwise profile

also bears a strong resemblance to the numerically computed steady, inviscid forced response to a moving surface pressure source, in figure 5(a) of Părău *et al.* (2007).

3.3. Time-dependent behaviour

In order to explore the time-dependent behaviour of the wave pattern, movies were taken with the camera mounted on the moving carriage but otherwise with the same orientation and backlighting configuration as used to obtain the images in figure 5 and the data in figures 6 and 7. The time-dependent behaviour of states I and II and of the transition region between these two states is shown in the plots of a_{max}/a_0 versus time in figure 11. Data are given for three values of $\epsilon = 0.30, 0.43$ and 0.51 , shown in figure 11(a–c), respectively, with curves for a number of values of α in each plot. The camera passes in front of a side column of the tank halfway through the carriage motion (from about 5 to 5.5 s), so there is a small gap in each of the curves. It should be noted that for the shadowgraph data reported in the previous section, the camera (which was stationary) was positioned about 30 cm beyond this column, so the data from the moving camera pass the stationary shadowgraph location at around $t = 7$ s.

For all the curves in figure 11, $a_{max}/a_0 = 1$ at $t = 0$, the instant when the carriage starts from rest. During the early part of the carriage acceleration ($t \lesssim 2.3$ s), the curves for each value of ϵ (each subplot) follow the same trajectory. The curves for the lowest value of α for each of the three values of ϵ are nearly steady after the start-up period ($0 \leq t \leq 4$ s) and this was confirmed from the images to be a state-I response. The curve for the highest value of α at each ϵ shows a similarly steady response and this was confirmed from the images to be a state-II response. It is interesting to note the narrow range of α between the state-I and state-II curves in each plot. For instance, in figure 11(a), $\epsilon = 0.30$, the difference between the highest value of α corresponding to a nearly steady state-I response and the lowest value corresponding to a nearly steady state-II response is only 4×10^{-3} (or about 0.01 cm s^{-1}). For $\epsilon = 0.51$, this transition region broadens; oscillations were observed over a range of $\Delta\alpha = 0.026$ (or about 0.6 cm s^{-1}). For values of α between those for the state-I and state-II responses, the curves show a regular oscillation whose period and amplitude increase with increasing α as state II is approached from below. The oscillation period is on the order of 1 s and the amplitude is sometimes as large as $\Delta a_{max}/a_0 = 2$, the typical jump between states I and II at the transition. Though this region between states I and II has been called a transition region above, it may actually be a separate state of unsteady response. Finally, it is admittedly sometimes difficult to determine precisely when the oscillations begin or end as α is varied. For example, an interesting event can be seen in the data with $\epsilon = 0.51$ and $\alpha = 0.884$ (figure 11c), where the wave pattern was observed to grow and become stable in state II, briefly transition back to state I, and then transition back to state II again.

The oscillations in figure 11 appear to decay with time, indicating that the oscillatory state may be transient. The period of the oscillations is large (~ 1 s) in comparison to the period of the linear capillary–gravity wave with minimum phase speed ($T_{min} = \sqrt{2\pi(\tau/\rho g^3)^{1/4}} \sim 0.07$ s) and persist even though the carriage travels on the order of seven oscillation periods during one run. To investigate whether the oscillations decay to zero, the shadowgraph lighting set-up was moved to allow movies to be recorded further down the tank from where the motion starts. Because of lighting limitations, the shadowgraph set-up could not capture both the start-up and later time motions in a single run. Figure 12 shows a plot of a_{max}/a_0 versus time for $\epsilon = 0.43$ and $\alpha = 0.905$, with the data from the extended run plotted with the

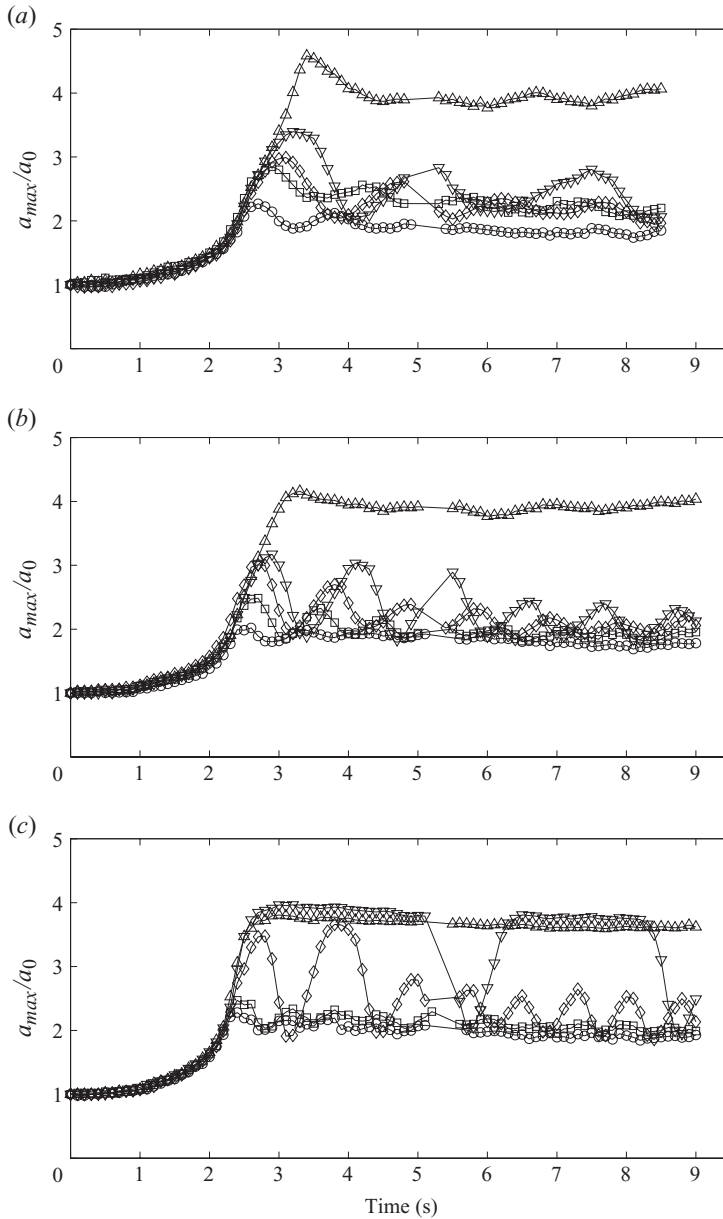


FIGURE 11. Plots of the normalized maximum depth of the surface depression, a_{max}'/a_0 , versus time for (a) $\epsilon = 0.30$, (b) $\epsilon = 0.43$ and (c) $\epsilon = 0.51$, for various values of α . (a) \circ , $\alpha = 0.927$; \square , $\alpha = 0.938$; \diamond , $\alpha = 0.940$; ∇ , $\alpha = 0.9440$; \triangle , $\alpha = 0.9444$. (b) \circ , $\alpha = 0.88$; \square , $\alpha = 0.89$; \diamond , $\alpha = 0.905$; ∇ , $\alpha = 0.907$; \triangle , $\alpha = 0.909$. (c) \circ , $\alpha = 0.856$; \square , $\alpha = 0.862$; \diamond , $\alpha = 0.873$; ∇ , $\alpha = 0.884$; \triangle , $\alpha = 0.888$.

original curve from figure 11 for comparison. The camera passes in front of another tank column between roughly 10 and 11 s, so there is another gap in the data. The figure shows that while the amplitude of the oscillations does decrease, it does not appear to reach zero, at least over the range measured. Furthermore, at late times, the oscillation period does not appear to be as regular as it was near the start-up.

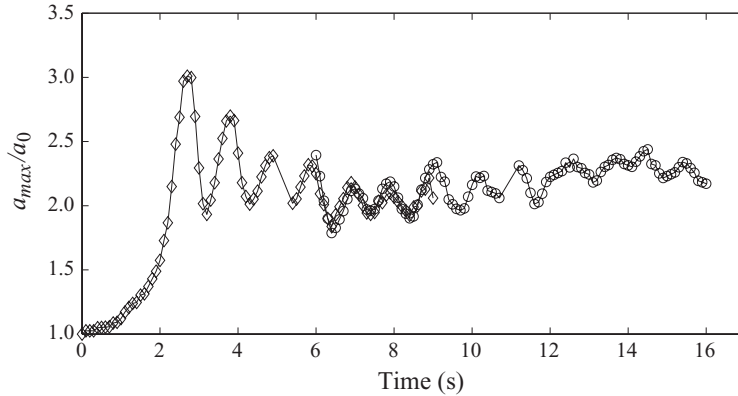


FIGURE 12. Plots of the normalized maximum depth of the surface depression, a_{max}/a_0 , versus time for $\epsilon = 0.43$ and $\alpha = 0.905$. The points marked by \diamond are the original data and those marked by \circ are the data from the extended run.

Unfortunately, the length of this data set reaches the physical limitations of our experimental facility. Also, the fact that the carriage height above the mean water level varies by about 1 mm over the extended length of the travel, might affect the oscillation slightly. Thus, whether or not the wave pattern settles to a steady state near the state I–II transition, given enough time, is still an open question.

A second type of unsteady behaviour occurs in state III. If one imagines successive experiments with increasing α in state II, one finds that the depth of the trailing depression diminishes while that of the forward depression increases. When state III is reached, the trailing depression is replaced by a V-shaped pattern with its vertex made up of the local depression under the air-jet tube. This pattern is unsteady and though it has a rather well-defined ‘cycle’ in time, it does not appear to be strictly periodic. Images during one of these cycles are shown with above-surface views and below-surface views in figures 13 ($\epsilon = 0.43$ and $\alpha = 0.981$) and 14 ($\epsilon = 0.51$ and $\alpha = 0.958$), respectively. In these image sequences the movie camera was mounted on the instrument carriage and, therefore, travelled along the tank with the air-jet tube. The temporal spacing between the images was 0.36 s in figure 13 and 0.2 s in figure 14.

As can be seen from the above-surface images in figure 13, the cycle begins with a ‘V’ shape as shown in figure 13(a). The pattern then stretches out as two lump-like depressions are shed from the tips of the V (figure 13b, c), producing a more localized response (figure 13d). The extended response quickly grows again and the V-shaped pattern is observed once more (figure 13e, f). A similar kind of shedding instability has been observed for shallow-water solitary waves governed by the KdV equation (Akylas 1984; Cole 1985; Wu 1987).

This growth and shedding cycle can also be seen using the below-surface view, as shown in figure 14. The pattern begins in figure 14(a) with an upstream depression directly underneath the air-jet tube followed by two side-by-side, smaller following depressions. This is the underwater view of the V-shaped pattern seen from above the surface in figure 13(a). The leading depression begins to deepen (figure 14b, c) and then takes on the appearance of the state-II pattern in the state I/II transition region (figure 5d). As the leading-depression depth increases, its speed decreases and the depression begins to move behind the air-jet tube (figure 14c, d). As this depression continues to move backwards, the initial trailing depression is ‘shed’

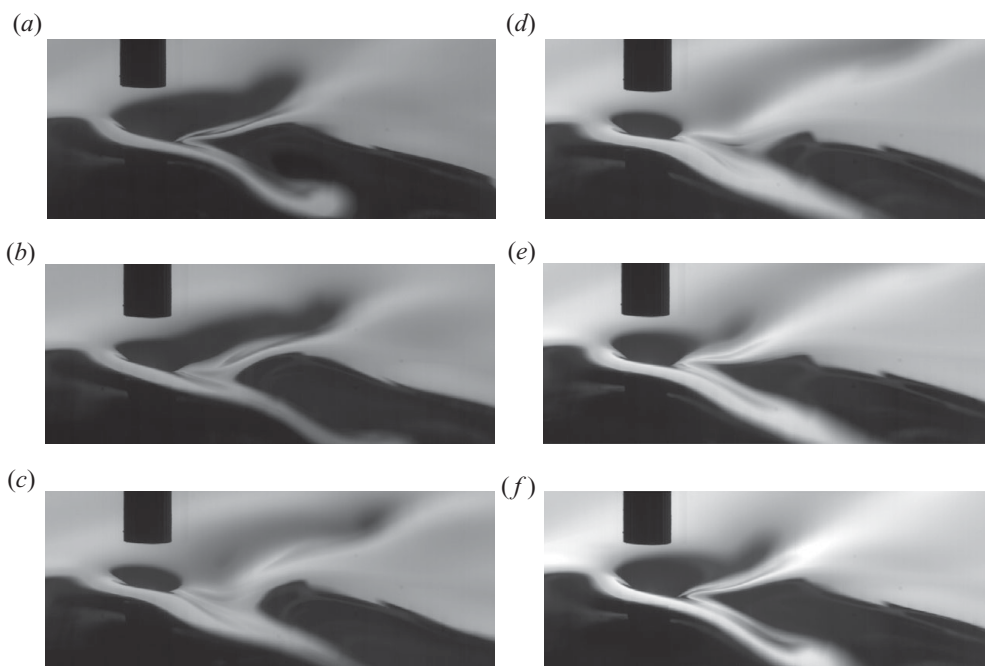


FIGURE 13. (a–f) Sequence of images showing the ‘shedding’ oscillation of the wave pattern in state III from above the surface for $\epsilon = 0.43$ and $\alpha = 0.981$. The images are separated by 0.36 s in time. From Diorio *et al.* (2009).

(figure 14e), and is eventually replaced by the backward-propagating upstream depression (figure 14f). The pattern then settles into a shape similar to its original configuration (figure 14g, h).

It is important to note that the boundary between states II and III is a bit fuzzy, as was the boundary between states I and II. At both boundaries, runs at the same nominal conditions can yield different responses. The above-described ‘shedding cycle’ at the states II–III boundary at first appears rather infrequently as the speed is increased from run to run, perhaps occurring only once in a given run. As the speed is increased further, this shedding cycle appears more frequently while the period of the cycle decreases. Finally, as $\alpha \rightarrow 1$, the wave pattern becomes highly extended.

4. Summary and conclusions

The deformation pattern generated by an isolated pressure distribution moving across a water surface at constant speed, U , was explored experimentally. The pressure distribution, which was created by blowing air onto the water surface from a vertically oriented tube, was set to move at speeds below the minimum phase speed, c_{min} , for linear gravity–capillary waves in deep water. The strength of the pressure source is characterized by the ratio $\epsilon = a_0/D$, where a_0 is the maximum depth in the dimple formed on the water surface when the air-jet tube is stationary and D is the inside diameter of the tube. For a given ϵ , as $\alpha = U/c_{min}$ is increased from a value well below $\alpha = 1$ in successive experiments, the surface deformation pattern transitions between several separate states. At low speed, the pattern consists of a nearly circular dimple directly under the air-jet tube; the shape of this dimple is nearly the same as that found when the air-jet tube is stationary. This type of response is called state I.

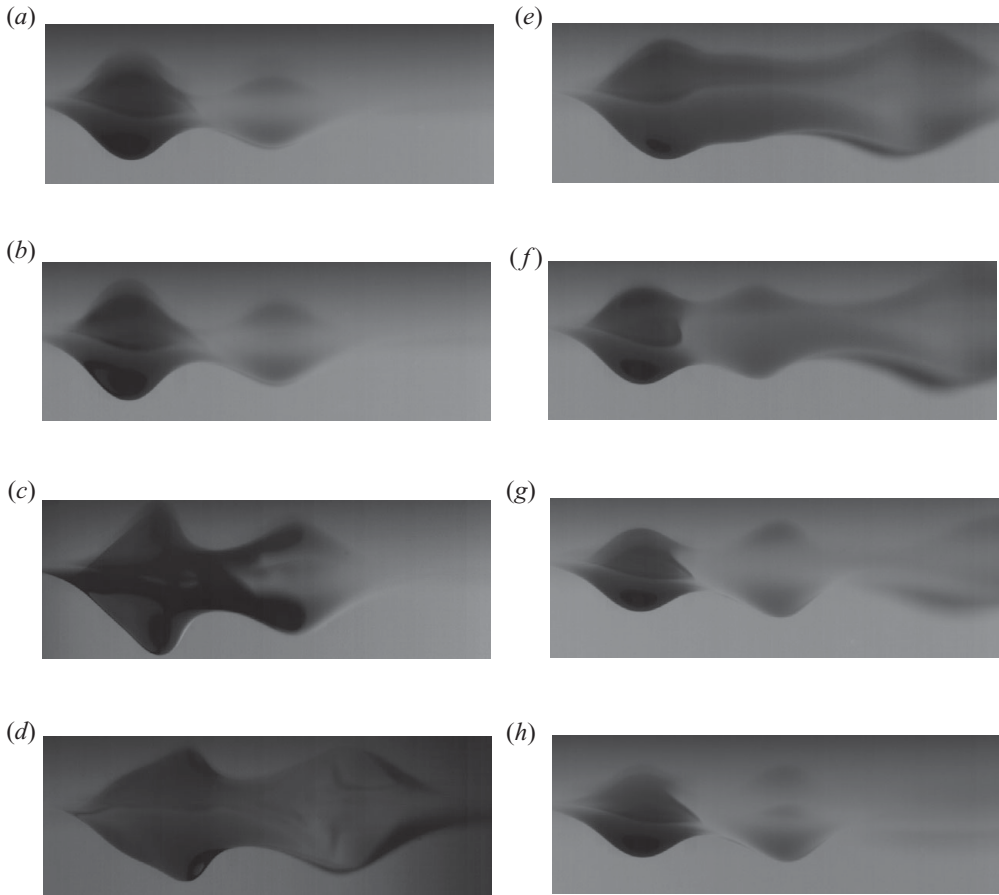


FIGURE 14. Sequential images showing the oscillation of the wave pattern for $\epsilon = 0.51$ and $\alpha = 0.958$ ($U = 22.22 \text{ cm s}^{-1}$). The images are separated by 0.2 s in time. (a) The V-shaped pattern begins to form. (b) The amplitude of the peak under the air-jet tube grows. (c) As the peak grows, it moves backwards (moving slower than the air-jet tube). (d) As the main peak moves back further, the trailing wave grows in amplitude, and is eventually ‘shed’ in (e). (f) A new trailing peak is formed and the pattern begins to retake its original shape, (g) and (h).

At higher speeds, the surface response consists of a local depression under the tube followed by a deeper depression that is elongated in the cross-stream direction. This type of surface deformation pattern is called state II. The boundary between states I and II is a region of oscillatory surface response and the amplitude and period of this oscillation increase as α is increased over a narrow band between the two states. The maximum depth of the surface deformation pattern, a_{max} , jumps by approximately $2a_0$ between states I and II. In state II, the trailing depression is geometrically similar to profiles of freely propagating gravity–capillary lumps computed on the basis of steady potential flow. As in these computations, it is found experimentally that a_{max} decreases with increasing α . Furthermore, the experimental results show that there is a single curve relating a_{max} and α for all values of ϵ , in qualitative agreement with the relationship between a_{max} and α found theoretically for free inviscid gravity–capillary lumps. Finally, as α approaches 1, a third response state consisting of a finite length V-shaped pattern appears. This pattern is unsteady and periodically sheds waves of depression, resembling gravity–capillary lumps, from the tips of the V.

We thank Dr E. Părău for making available as yet unpublished numerical results on lumps. This work was supported by NSF (grants DMS-0604416, DMS-098122 and OCE-751853), AFSOR (grant FA9550-07-0005) and the ARCS Foundation. We also thank Andrew Lisiewski, Ryan Harris, Nick Watkins and Joseph Zuech for their help with these experiments.

REFERENCES

- AKERS, B. & MILEWSKI, P. A. 2009 A model equation for wavepacket solitary waves arising from capillary–gravity flows. *Stud. Appl. Math.* **122**, 249–274.
- AKYLAS, T. R. 1984 On the excitation of long nonlinear water waves by a moving pressure distribution. *J. Fluid Mech.* **141**, 455–456.
- AKYLAS, T. R. 1993 Envelope solitons with stationary crests. *Phys. Fluids A* **5**, 789–791.
- AKYLAS, T. R. 1994 Three-dimensional long water–water phenomena. *Annu. Rev. Fluid Mech.* **26**, 191–210.
- AKYLAS, T. R. & CHO, Y. 2008 On the stability of lumps and wave collapse in water waves. *Phil. Trans. R. Soc. Lond. A* **366**, 2761–2744.
- CALVO, D. C. & AKYLAS, T. R. 2002 Stability of steep gravity–capillary solitary waves in deep water. *J. Fluid Mech.* **452**, 123–143.
- CHO, Y., DIORIO, J. D., AKYLAS, T. R. & DUNCAN, J. H. 2011 Resonantly forced gravity – capillary lumps on deep water. Part 2. Theoretical model. *J. fluid Mech.* **672**, 288–306.
- COLE, S. L. 1985 Transient waves produced by flow past a bump. *Wave Motion* **7**, 579–587.
- DIAS, F. & IOOSS, G. 1993 Capillary–gravity solitary waves with damped oscillations. *Physica D* **65** (4), 399–423.
- DIAS, F. & KHARIF, C. 1999 Nonlinear gravity and capillary–gravity waves. *Annu. Rev. Fluid Mech.* **31**, 301–346.
- DIORIO, J. D., CHO, Y., DUNCAN, J. H. & AKYLAS, T. R. 2009 Gravity–capillary lumps generated by a moving pressure source. *Phys. Rev. Lett.* **103**, 214502.
- GRIMSHAW, R. H. J. (Ed.) 2007 *Solitary Waves in Fluids*. WIT Press.
- KIM, B. & AKYLAS, T. R. 2005 On gravity–capillary lumps. *J. Fluid Mech.* **540**, 337–351.
- KIM, B. & AKYLAS, T. R. 2007 Transverse instability of gravity–capillary solitary waves. *J. Engng Math.* **58**, 167–175.
- LAMB, H. 1993 *Hydrodynamics*, 6th edn. Cambridge University Press.
- LONGUET-HIGGINS, M. S. 1989 Capillary–gravity waves of solitary type on deep water. *J. Fluid Mech.* **200**, 451–470.
- LONGUET-HIGGINS, M. S. 1993 Capillary–gravity waves of solitary type and envelope solitons on deep water. *J. Fluid Mech.* **252**, 703–711.
- LONGUET-HIGGINS, M. S. & ZHANG, X. 1997 Experiments on capillary–gravity waves of solitary type on deep water. *Phys. Fluids* **9**, 1963–1968.
- PĂRĂU, E., VANDEN-BROECK, J.-M. & COOKER, M. J. 2005 Nonlinear three-dimensional gravity–capillary solitary waves. *J. Fluid Mech.* **536**, 99–105.
- PĂRĂU, E., VANDEN-BROECK, J.-M. & COOKER, M. J. 2007 Three-dimensional capillary–gravity waves generated by a moving disturbance. *Phys. Fluids* **19**, 082102.
- RAPHAËL, E. & DE GENNES, P. G. 1996 Capillary–gravity waves caused by a moving disturbance: wave resistance. *Phys. Rev. E* **53**, 3448–3455.
- RUSSELL, J. S. 1844 Report on Waves, Fourteenth Meeting of the British Association for the Advancement of Science, 311–390.
- VANDEN-BROECK, J.-M. & DIAS, F. 1992 Gravity–capillary solitary waves in water of infinite depth and related free-surface flows. *J. Fluid Mech.* **240**, 549–557.
- WHITHAM, G. B. 1974 *Linear and Nonlinear Waves*. Wiley-Interscience.
- WU, T. Y. T. 1987 Generation of upstream advancing solitons by moving disturbances. *J. Fluid Mech.* **184**, 75–99.
- ZHANG, X. 1995 Capillary–gravity and capillary waves generated in a wind-wave tank: observations and theories. *J. Fluid Mech.* **289**, 51–82.